HYDROXYL TAGGING VELOCIMETRY (HTV) IN HIGHLY ACCELERATED FLOWS

By

Amber Nicole Perkins

Thesis

Submitted to the Faculty of the

Graduate School of Vanderbilt University

in partial fulfillment of the requirements

for the degree of

MASTER OF SCIENCE

in

Mechanical Engineering

December, 2011

Nashville, Tennessee

Approved:

Joseph A. Wehrmeyer

Don G. Walker

Robert W. Pitz

ACKNOWLEDGEMENTS

This work was supported by Arnold Engineering Development Center under contract No. F40600-03-D-001. I would like to thank Dr. Joseph Wehrmeyer and Dr. Robert Pitz for their assistance and support. I would also like to thank Marc C. Ramsey for his efforts. Last, but certainly not least, I would like to thank my mother Joy Guthrie for supporting me and helping me to see the end in the beginning.

TABLE OF CONTENTS

Page

LIST OF TABLES

LIST OF FIGURES

CHAPTER I

INTRODUCTION

1.1 Laser Diagnostic Techniques to Measure Gas Velocity

Non-intrusive velocity measurements in gas flowfields have recently been performed with molecular tags that do not require the addition of particles to the gas flow (Alexander 2008; Blandford 2008; Ismailov 2006; Mittal 2009). An alternative to these molecular velocity measurements are particle methods such as particle velocimetry (PIV) where particle displacements are measured and related to the gas velocity (Fajardo 2009; Timmerman 2009). In PIV, particles are seeded uniformly into the gas and the particle must closely follow the gas flow (Ismailov 2006). PIV is undesirable in gas flows where the flow is highly accelerated and swirled such that the particle velocity differs from the gas velocity. In jet engine test facilities, the addition of particles is prohibited and the rapid acceleration of the gas through the nozzle requires an alternative method. Thus molecular tagging velocimetry is a preferable alternative to particle methods to measure velocity non-intrusively in jet engine exhausts.

Molecular tagging velocimetry (MTV) is sometimes used to characterize fluid flows (Alexander 2008; Blandford 2008; Ismailov 2006; Mittal 2009; Sitjsema 2002). MTV has been employed by several researchers to examine in-cylinder cold flow characteristics of optical engines by premixing biacetyl into a nitrogen gas flow, exciting the biacetyl phosphorescence in a grid pattern with a 308 nm XeCl excimer laser, and tracking the luminance grid to determine the velocity (Mittal 2009; Stier 1999; Ismailov 2006). However, the biacetyl tag method is limited to the study of cold oxygen-free

gases due to phosphorescence quenching by oxygen. Another MTV technique applied by Miles et al. (2000), uses the vibrational excitation of oxygen molecules by Raman excitation followed by interrogation using laser-induced electronic fluorescence (RELIEF) to examine the velocity. The application of RELIEF to high-temperature combustion exhausts is problematic due to the natural presence of vibrationally excited oxygen that obscures the tagged lines. Grids of NO have been created to measure velocity by MTV using seeded and unseeded techniques. NO_2 can be seeded into a gas flow and subsequently dissociated to form a grid of NO (Hsu 2009). However, the NO_2 gas will rapidly decompose in the high-temperature regions of combustion devices. In the air photolysis and recombination tracking (APART) method, a focused ArF excimer laser forms a short tag line (~1 cm) from air in the focal region (Sijtsema 2002).

In Hydroxyl Tagging Velocimetry (HTV), an OH tag is created by dissociating the water vapor naturally present in the flow thus eliminating the need for insertion of a molecular species for tagging (Ribarov 2002; Pitz 2000). In addition, the OH tag persists at high temperature conditions (Wehrmeyer 1999). The HTV technique creates a grid of hydroxyl radicals (OH) by photodissociation of water vapor via a 193-nm ArF excimer laser. The H_2O photodissociation by the 193-nm laser is a single photon process that can create long OH tag lines. After creating an OH grid, the grid is imaged at zero time (undisplaced) and a later time (displaced), as seen in Figure 1. The velocity is calculated by measuring the individual displacements within the molecular grid and dividing by the time interval between the writing and reading processes.

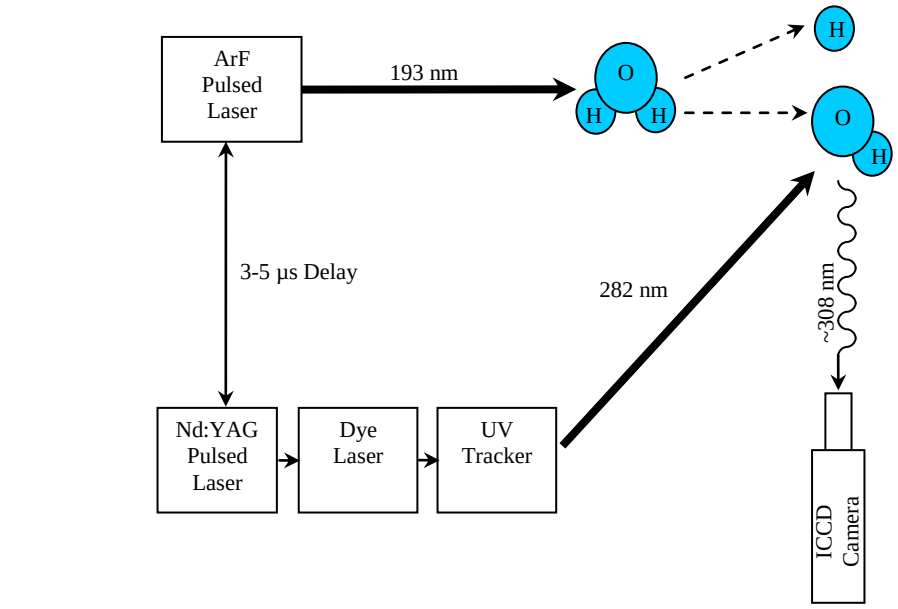

(a)

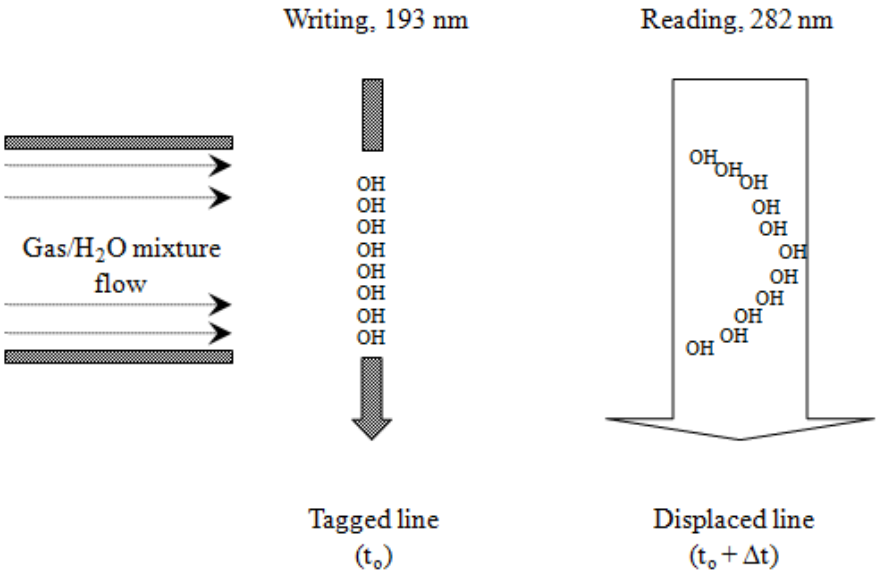

(b)

Figure 1. (a) Schematic showing hydroxyl production (193-nm), excitation (282-nm), and imaging (b) Schematic showing grid tracking process.

1.2 Previous HTV work

Previously, HTV has been applied to supersonic air flow over a cavity in a research cell; HTV images were recorded with a signal-to-noise ration (SNR) of ~10 to obtain instantaneous velocity measurements with a precision of ~1% in the ~680 m/s free stream (Pitz 2005; Lahr 2010). Applications of HTV to engine test cell environments are more difficult due to test cell vibrations and reduced light collection at longer light collection distances. In a previous application of HTV to a J85-GE-5 jet engine exhaust, velocity measurements were made in the centerline at full throttle conditions yielding a mean velocity of ~540 m/s and a rms variation of ~5% (Blandford 2008; Alexander 2008). In these previous J85 jet engine tests, the displaced HTV image was instantaneously measured and compared to an undisplaced HTV image previously recorded before the engine is fired; consequently, vibration of the optical setup would contribute to the rms variation measurement (Blandford 2008; Alexander 2008).

1.3 HTV in turbojet engine exhaust

In Chapter II, HTV is applied to a turbojet engine exhaust and images are recorded with an intensified interline-transfer CCD camera operating in dual-pulse mode. The dual-pulse feature allows for imaging of the initial and displaced grids in quick succession to create image pairs for analysis. The engine vibrations cause the camera to move with respect to the initial grid. This relative movement creates error in determining the initial placement of the grid, when using a single image camera. The dual pulse imaging technique is likely to have the advantage of reducing the effects of engine vibrations on the velocity error.

1.4 HTV in shock tube flow

In Chapter III, HTV is applied to a shock tube flow to contribute to previous measurements taken by Smith et al. (1994) in the same facility. The shock tube study aims to determine the velocity downstream of the initial shock wave. In conjunction with pressure transducers placed along the length of the tube to determine shock speed, HTV images are analyzed using a spatial correlation technique to determine displacements of the grid intersections and thereby the two-dimensional velocity distribution downstream of the initial shock wave. These measurements provide a preliminary means for exploring the possibilities of validating theoretical codes and CFD.

CHAPTER II

HYDROXYL TAGGING VELOCIMETRY APPLIED TO JET ENGINE

2.1 Engine Facility

The HTV measurements were conducted on a General Electric J85-GE-5 turbojet engine mounted on a portable test stand located at the Propulsion Research Facility at the University of Tennessee Space Institute in Tullahoma, TN. The J85-GE-5 is a single-shaft turbojet engine used in the T38 military plane. It is composed of an eight-stage axial-flow compressor powered by two turbine stages and can produce up to 2,400 lbf of thrust and 3,600 lbf in afterburner (augmented) mode. The engine is used as a test bed to develop and evaluate intrusive and non-intrusive instrumentation before they are applied to larger engines and facilities (Alexander 2008). For the current study, the engine is not

tested in augmented mode due to absorption of the tag lines by one or more gas species (Alexander 2008).

2.2 Experimental System

A tunable 193-nm ArF excimer laser (Lambda Physik COMPex 150-T, 193-194 nm) with output energy of 150 mJ per pulse, 0.2 mrad divergence, and a pulse duration of 20 ns was used to photodissociate the water vapor to produce OH radicals. The ArF laser was operated in broadband mode at 193.4 nm (0.5 nm bandwidth). The ArF beam, 20 mm high by 10 mm wide, was split via a beam splitter and sent into grid forming optics. The grid forming optics consist of two sets of optics closely spaced: a 300 mm focal length cylindrical lens (25 mm x 40 mm) and a stack of eleven cylindrical lenses (20 mm long x 2 mm wide). Each set of grid optics forms 11 parallel beams with energy of ~2.0 mJ/beam and spacing of about 2 mm. The two sets of 11 beams are crossed at a 24º angle. A schematic showing the engine exhaust, tag lines, and camera field of view is shown in Figure 2.

The OH radicals were excited by a Nd:YAG (Continuum Lasers Powerlite 9010) pumped tunable dye laser with an ultraviolet wavelength extender. The doubled output of the dye laser is tuned to excite the strong $Q_1(1)$ line in the $A^2\Sigma^+$ $(v'=1)\leftarrow X^2\Pi_i$ $(v''=0)$ OH band at a wavelength of 281.997 nm (35461.330 cm^{-1}). The $Q_1(1)$ line was chosen in order to be able to visualize the OH fluorescence under both cold air and hot combustion exhaust conditions (Ribarov 2005). The dye laser wavelength and the $Q_1(1)$ line position was determined by fluorescence excitation spectra taken in room air and in a propane torch as done previously (Pitz 2005; Ribarov 2005). The ~282 nm beam (~7 mJ/pulse)

was expanded by a negative cylindrical lens (focal length ≅ -150 mm) and focused into a sheet 25 mm wide by 0.5 mm thick with a 1000 mm focal length spherical lens.

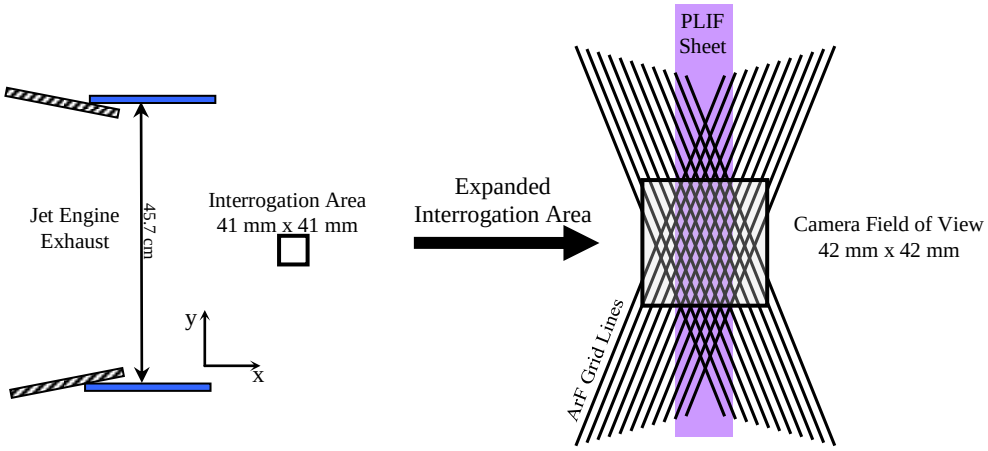

Figure 2. Schematic showing engine exhaust, tag lines, and camera field of view (with the interrogation area drawn to scale on left and an expanded view on the right).

The images were recorded using an intensified interline CCD dual-pulse camera (Princeton Instruments PI-MAX II 1024x1024 pixels). The dual-pulse feature takes advantage of the camera's ability to acquire a second image, the displaced image, while the first image, the undisplaced image, is being read out. As soon as the first image is acquired, it is shifted and held. The second exposure begins and is held in the active area until the first image is read out. The fluorescence light was collected by a 105 mm focal length f/4.5 UV Nikon camera lens positioned above the jet engine exhaust at the nozzle exit. To capture the OH fluorescence near ~305-325 nm and block interfering background light from the lasers (193-nm, 282-nm), a Schott UG-11 (1 mm thick) filter and a WG305 (3 mm thick) filter were used in front of the camera lens to create a

bandpass filter from 305-375 nm. Operating in dual-pulse mode, the camera captures images in quick succession (minimum separation time of 2 µs): one of the undisplaced grid and the other of the displaced grid. Figure 3 shows the timing schematic with respect to the firing of the YAG laser and the two camera gates. The first camera gate captures the undisplaced grid, while the second camera gate captures the displaced image. To increase the data acquisition rate during the engine test, the camera pixels were binned 4x4 during the camera read-out process to give a final image with a 256x256 pixel format. The camera image was calibrated by placing a ruler in the focal plane giving a factor of 6.16±0.02 pix/mm that is used to determine displacements. The 256x256 pixel images corresponded to a 41.6 mm x 41.6 mm area in the jet engine exhaust.

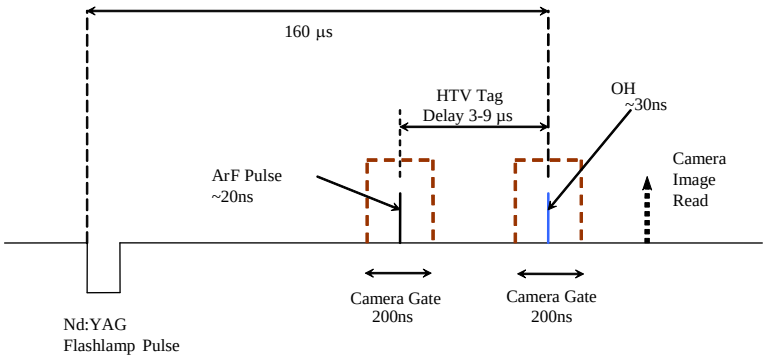

Figure 3. Timing schematic for dual-pulse imaging.

2.3 Test Conditions

The HTV measurements were performed to determine the centerline velocities at the closest access point of the jet engine exhaust. The engine testing was performed for

six engine conditions ranging from idle to full throttle. In Table 1, the six engine conditions; delay times between the write and read lasers and the average measured centerline displacement are shown. Time delays were taken at 0, 3, 5, 7, and 9 μs delays for each throttle condition. The time delays reported are chosen to keep the grid displacement less than the grid spacing (~2 mm) to prevent ambiguity in computing the grid movement. At the higher throttle settings, the delay time was decreased from 9 μs to 3 μs to keep the displacement below 2 mm. With these short time delays (3-9 μs), the effects of optical vibrations and beam wandering induced by the engine vibrations on the displacement of the tagged grid over the delay time is eliminated as the equipment vibrations at 100,000 Hz are negligible.

A harmonic analysis can be performed to verify that optical equipment vibrations are less than 100,000Hz. Consider an aluminum optic mount attached to a stainless steel post. The natural frequency of the system, given by

$$f_n = \frac{1}{2\pi}\sqrt{\frac{k}{m}} \tag{1}$$

where, k is the stiffness and m is the mass of the system. The stiffness is given by

$$k = \frac{EA_o}{L} \tag{2}$$

where, E is the modulus of elasticity, A_o the cross-sectional area, and L is the length of the optic mount and post (Gere 1997). Using a stiffness value of 1.92×10^{10} kg/s^2 and a mass of 0.2402 kg for the system, optical post and mount, the natural frequency of is found to be ~45,000 Hz. Given this value, the optical equipment vibrations are negligible. Engine vibrations, however, can still cause optical misalignments that reduce the HTV image quality. Engine vibrations are transferred to the optics table that leads to

movement of the optics. This includes the possibility for the misalignment of the read beam, 282 nm sheet, with the write beam, 193 nm light. This results in an image with an indiscernible grid.

Table 1. Engine test conditions, delay times, and average centerline displacements using the dual-pulse method

Engine Setting	Delay time Δt (μs)	Displacement (pixels)	Displacement (mm)
1	9	4.21	0.68
2	9	5.87	0.95
3	9	9.82	1.59
4	3	4.45	0.72
5	3	7.30	1.19
6	3	10.84	1.76

Figure 4 shows image pairs, the undisplaced (0 μs) and displaced (3-9 μs) HTV images for the six engine conditions in Table 1. The undisplaced image (0 μs) is recorded from ArF excimer laser-induced fluorescence recorded by the ICCD camera through the filter (305-375 nm). This fluorescence comes from 193-nm excitation of fuel or fuel-derived species. Although O_2 LIF is produced by the ArF excimer laser, the filter (305-375 nm transmittance) blocks the O_2 LIF (Lee 1986). The whole grid with the camera view (41.6 mm x 41.6 mm) can be seen. In room air, the undisplaced grid pattern cannot be seen because the WG305 filter blocks the room temperature O_2 fluorescence from the ArF laser. The displaced grid, however, can be seen in room air due to illumination by the 282 nm light. The displaced image (3-9 μs) is the center portion of the OH grid that is revealed by the 282-nm laser sheet (25 mm wide). The flow direction of the image is toward the right of the image. The displaced grid moves a distance less than 2 mm from the initial position. With this displacement and time delay of 3 μs, a measured velocity of approximately 580 m/s is determined for the full throttle condition.

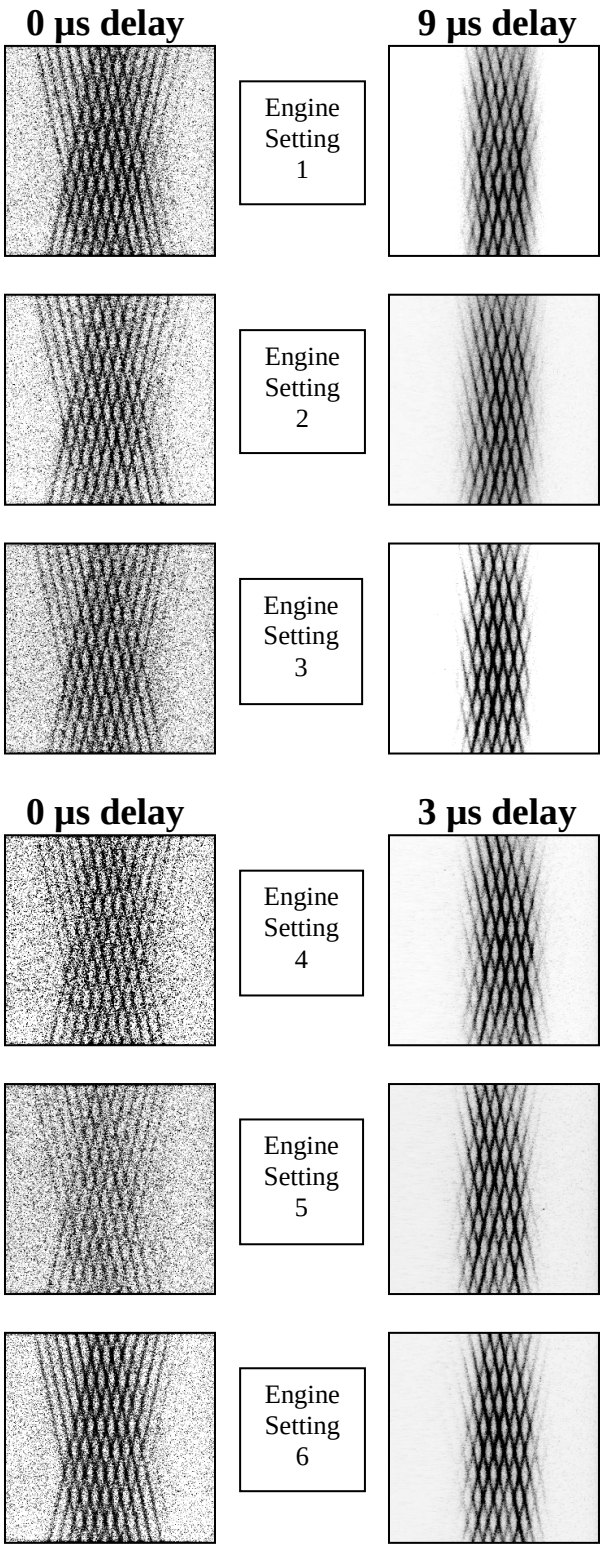

Figure 4. HTV dual-pulse images (41.6 mm x 41.6 mm) at each throttle condition [undisplaced (0 µs) and displaced (3-9 µs)].

2.4 Post-processing

Once the images were obtained, a spatial correlation method developed by Gendrich and Koochesfahani (1999) was used to determine the displacements of the grid intersections. With this method, various types of laser tagging patterns can be accommodated to yield high sub-pixel accuracy at short time delays between two images. The method employs a direct digital spatial correlation technique. A small window, referred to as the source window is selected from a tagged undisplaced image (Figure 5a), and is correlated with a larger roam window in the displaced image. The roam window is centered about the original location of the source window. The scheme calculates a spatial correlation coefficient between the intensity field of the source window and the roam window. The location of the peak of the correlation coefficient is identified as the displacement vector, which after division by Δt provides the estimate of the spatial average of the velocity within the source window. As indicated in Figure 5b, the velocity vector is drawn from the center of the source window to the center of the roam window with the peak correlation coefficient. In this work, the center of the roam window is located very near the center of each undisplaced line intersection. However, the velocity vectors are drawn between the centers of the source and roam windows with the highest correlation coefficient. Thus, the velocity vectors are not necessarily drawn between the exact centers of the undisplaced and displaced line crossings.

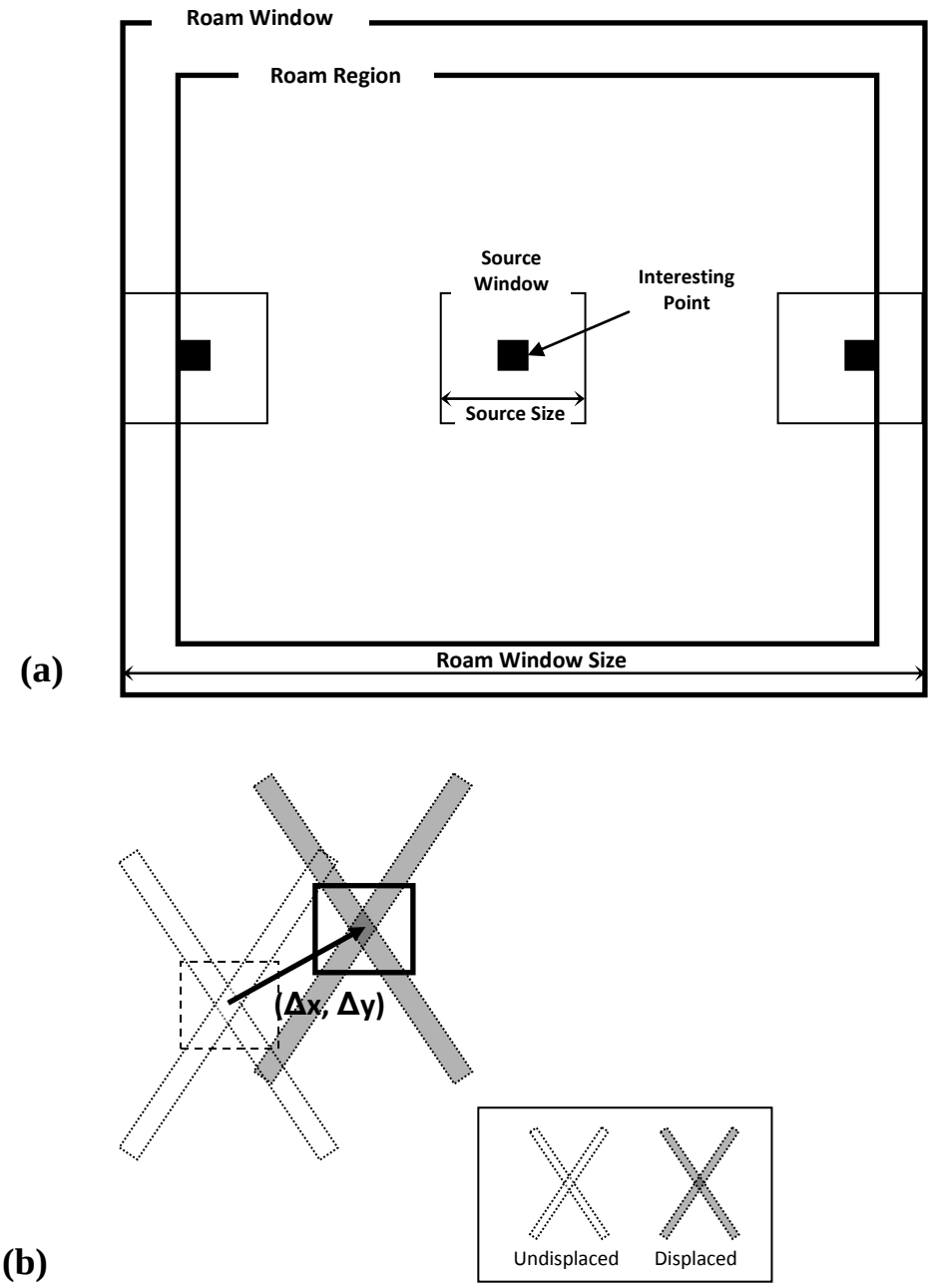

Figure 5. (a) Special correlation software depiction showing source and roam windows (b) Displacement vector determination

In Figure 6, a segment from a vertical section at x=21.8 mm, from the 9μs delay for engine setting 1 in Figure 4, defines the signal and noise used to determine the SNR value. The signal is obtained by fitting a Gaussian curve to the line out data as depicted. The noise value is determined by a residual value that is a difference between the data and the Gaussian fit. The SNR values of the undisplaced images are very low (typically less than about 0.7). The SNR of the displaced images were slightly higher at about 1.4. The 193-nm laser-induced fluorescence signal from the fuel is determined from the undisplaced images and is depicted in Figure 7. The fuel signal is determined by using the information obtained from the signal values less the value of the background value. The fuel signal is in terms of an arbitrary pixel intensity. The fuel signal value provides the best indicator of the fuel fluorescence. The fuel signal decreases with increasing throttle setting due to less unburnt fuel being present in the flow as the throttle setting increases.

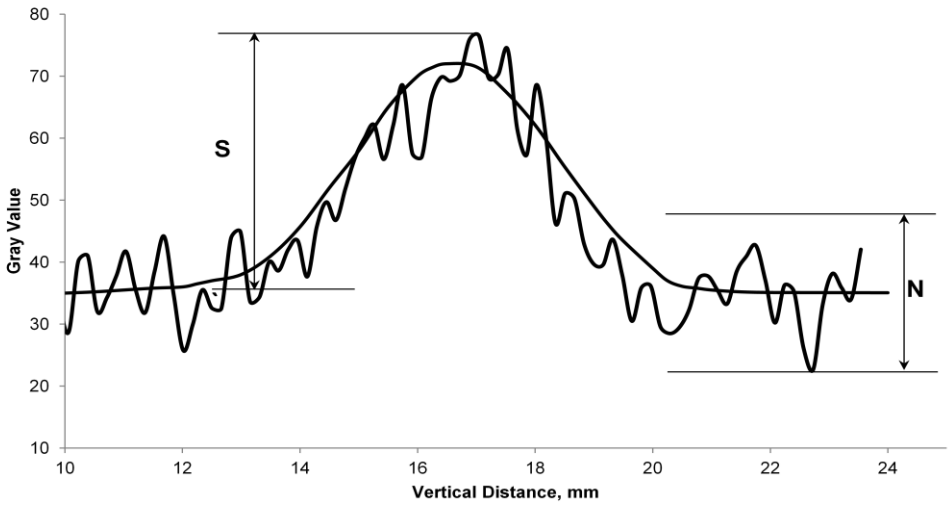

Figure 6. SNR definition. (From a vertical line out at x=21.8 mm) To moderate the influence of outliers (such as faulty pixels), N is estimated by 6 standard deviations, an interval which contains about 99% of normally distributed noise.

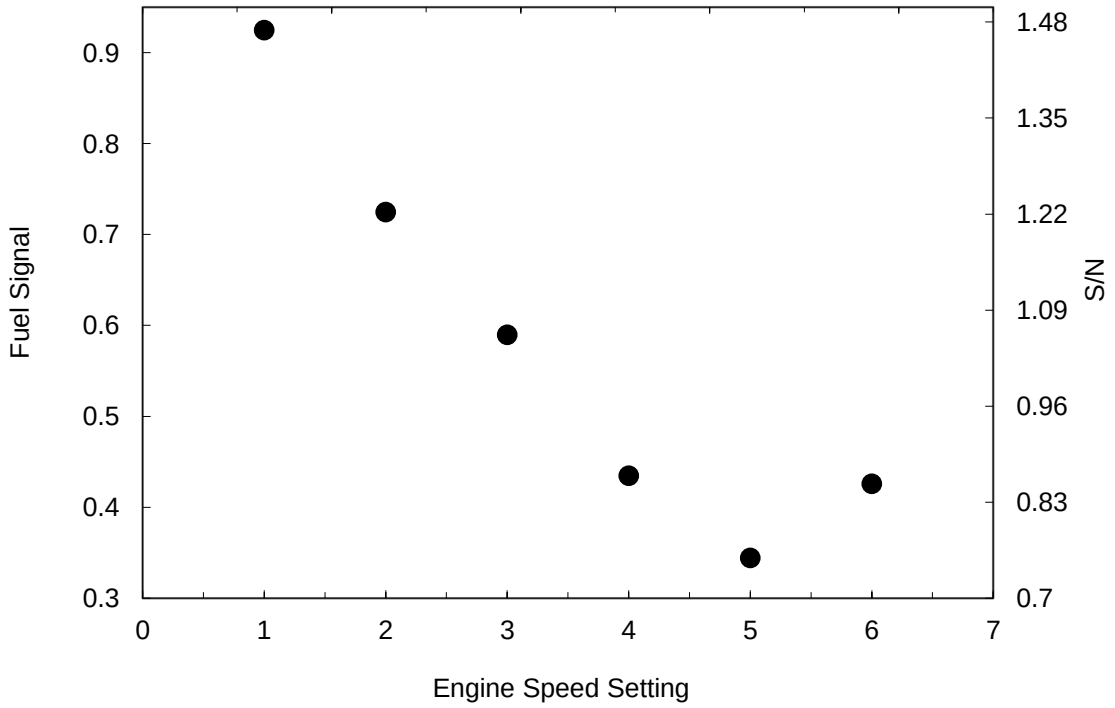

Figure 7. Fuel signal derived from 193-nm laser-induced fluorescence

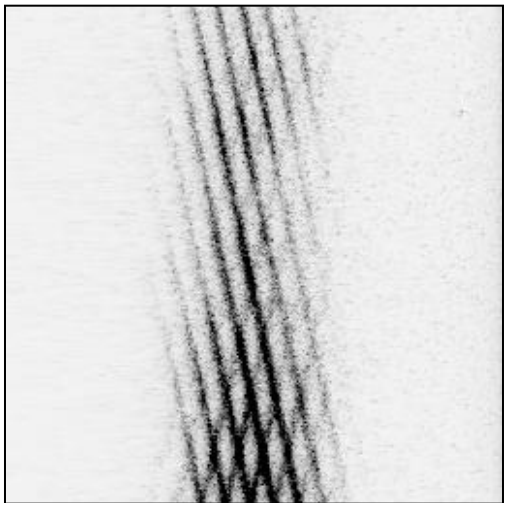

Figure 8. Displaced HTV image (3 µs time delay) where read sheet is out of plane

Table 2. Image pairs and intersection

Engine Setting	No. Image Pairs	Grid Intersections Specified	No. Possible Intersections	No. Actual Intersections Located
1	20	38	760	364
2	20	33	660	364
3	20	38	760	259
4	20	33	660	203
5	20	32	640	154
6	20	37	740	310

Table 2 represents the number of image pairs, number of intersections per image, possible resulting intersections, and the actual intersections found. A total of 50 image pairs were obtained for each throttle setting. Due to optical vibration, the read sheet moved out of the plane of interest in some images (Figure 8); thus they were not usable. For each condition, the 20 best images were chosen for analysis. The number of usable intersections is dependent on the ability of the software to correlate the intersections in the source and roam windows with a sufficiently high correlation coefficient value. The low number of actual intersections located by the software can be attributed to the low values of signal-to-noise in the images.

Figure 9 illustrates the velocity vectors obtained from averaging the HTV data at each point for engine setting 3. In this depiction, the average velocity is 177 m/s for the centerline flow of the engine exhaust at the nozzle exit. The velocity vectors from Figure 9 are superimposed on an undisplaced image in Figure 10. Figure 10b, a small region denoted in Figure 10a is expanded to see the velocity vectors better. Most of the displacement errors are in the y direction due to the elongated nature of the cross-sections formed at 24º. For the 24º crossings, the spatial correlation program can determine the horizontal displacement about 10 times more accurately than the vertical direction (Gendrich 1999).

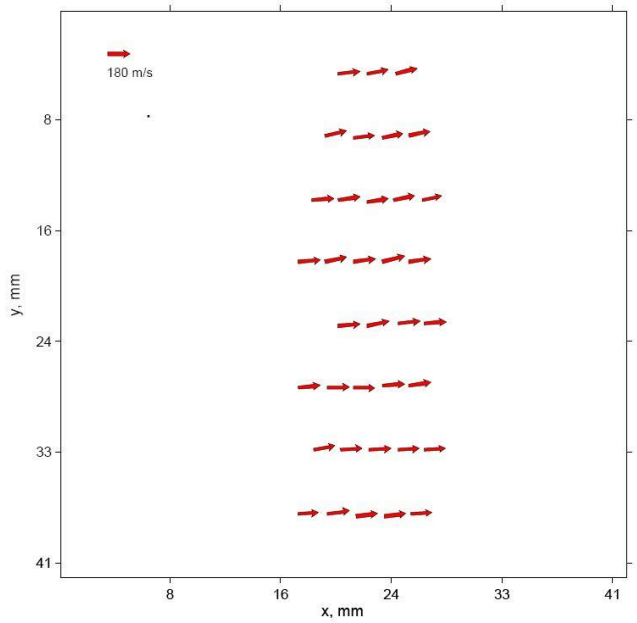

Figure 9. HTV derived centerline velocity vectors for engine setting 3 at the nozzle exit.

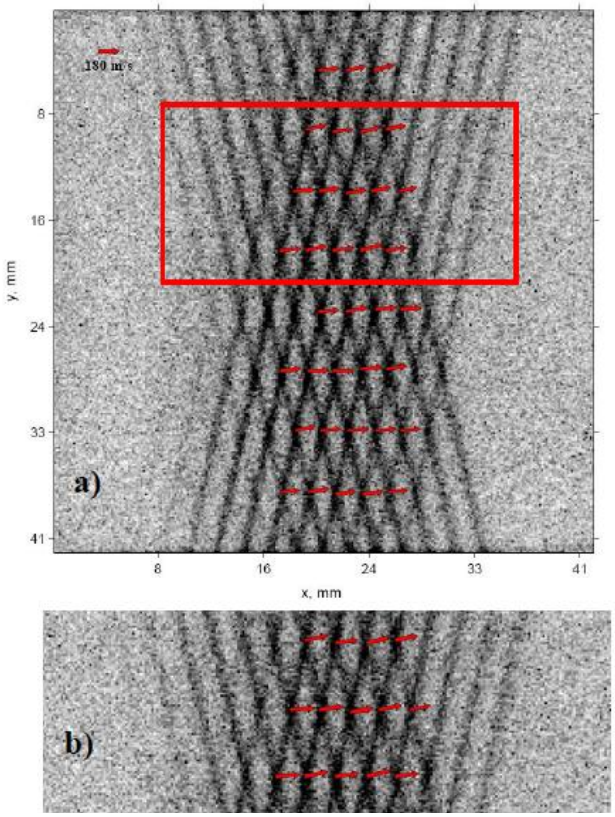

Figure 10. HTV derived centerline velocity vectors for engine setting 3 superimposed on an undisplaced image (a) velocity magnitude and (b) expanded view of velocity magnitude

2.4.1 Uncertainty

The uncertainty in the velocity data depends on two factors: uncertainty in timing between the write-read lasers, Δt, and the uncertainty in measuring the displacement, d, as follows:

$$\frac{\sigma_v}{v} = \left[\left(\frac{\sigma_d}{d} \right)^2 + \left(\frac{\sigma_{\Delta t}}{\Delta t} \right)^2 \right]^{1/2} \cong \frac{\sigma_d}{d} \tag{3}$$

where σ_i is the rms deviation of the ith quantity, v is the velocity, d is the displacement and Δt is the time delay. The timing uncertainty between the firing of the two lasers is ±5 ns due to electronics jitter over the time delay of 3-9 µs. Thus the timing uncertainty is less than 0.2% and can be neglected compared to the displacement error. Based on the calculations of Gendrich and Koochesfahani (1999), the uncertainty in determining the displacement for images of SNR ≅ 2 would be about 0.5 pixels for a displacement measurement in the x (centerline) direction shown in Figure 9. So for the average displacement of 9.82 pixels, this would result in 5% accuracy.

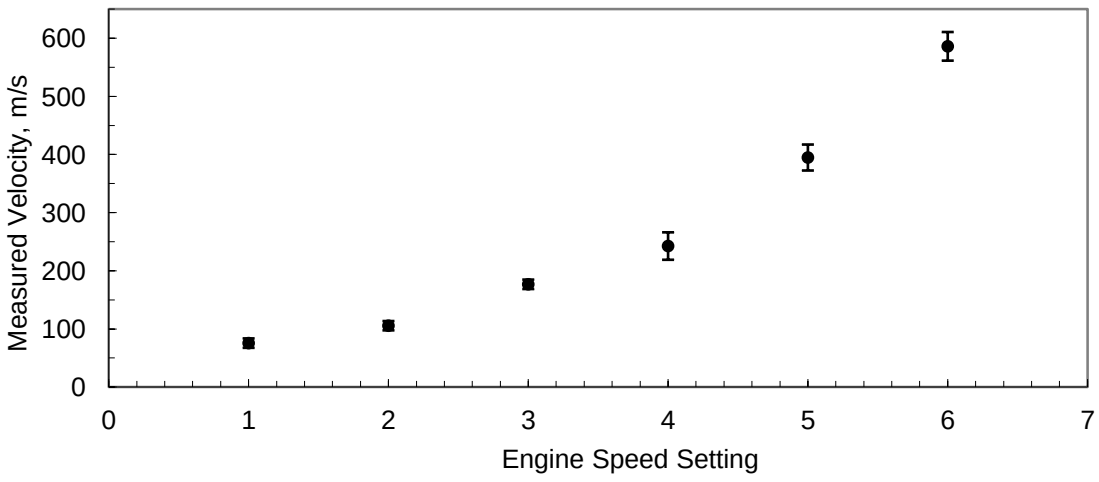

Figure 11. Measured velocity derived from HTV data.

2.5 Dual-pulse and single image method comparison

The measured average and rms deviation of the velocity versus engine speed for the dual-pulse method are displayed in Figure 11. The error bars indicate the rms deviation velocities. The measured average velocity is velocity in the x (centerline) direction. At the idle condition a velocity magnitude of 76 m/s is measured and the velocity ramps up to a value of 580 m/s at full throttle.

This study provided a means for comparing the previous single-image method to the current dual-pulse method. The single image method, utilized by Blandford et al. (2008), was executed by marking both the undisplaced (0 μs) and displaced image with OH fluorescence. With this method, one undisplaced image is taken prior to the engine test and is used with each displaced image. Alternatively, the dual-pulse method employs the use of image pairs taken in quick succession to determine velocity. To simulate the single-image method, one undisplaced image from the group of image pairs was chosen and used for analysis with each delayed image. The resulting comparison is portrayed in Figure 12. Displayed are the velocity rms deviations from the mean in percent. From this comparison, it can be seen that using the dual-pulse method results in a lower rms deviation from the mean. This is attributed to reducing the effect of engine vibration. There is about a 20% reduction in rms velocity deviation with respect to the mean velocity across the entire range. The largest reductions in the absolute value of the rms are at engine setting 1 and engine setting 4 where the grid displacement is the smallest (~0.7 mm from Table 1); for example, at engine setting 4 the rms is reduced from 13% to 9.7% by using the dual-pulse method. The most accurate HTV measurement is at full

throttle (engine setting 6) where the displacement is the longest at ~1.8 mm and the measurement uncertainty is about 4% for the dual-pulse method.

The major error in the velocity measurement is in the determination of the grid displacement for the low signal grids. If most of the rms velocity deviation is due to error in measurement of the grid displacement, the rms velocity should follow Equation (3) ($\sigma_v/v = \sigma_d/d$). Figure 13 gives the rms velocity deviations versus the reciprocal of the pixel displacements given in Table 1. From the rms velocity percent deviation, a pixel displacement error can be estimated. Two trend lines with slopes of 0.45 and 0.55 (for the dual-pulse and single-image methods, respectively are plotted. As can be seen, the points for each throttle setting lie closely to these lines, indicating that the average uncertainty in determining the displacement is ±0.55 pixels for the single-image method and ±0.45 pixels for the dual-pulse method. The elimination of vibration effects leads to a reduction of error from 0.55 to 0.45 pixels, which is a 20% relative decrease. Since errors add like the sum of squares [i.e., see Equation (3)], the vibration error corresponds to an rms value of 0.3 pixels (~50 microns). It appears that the rms velocity in the measurement in mostly a result of the displacement measurement error due to the low signal-to-noise of the HTV images.

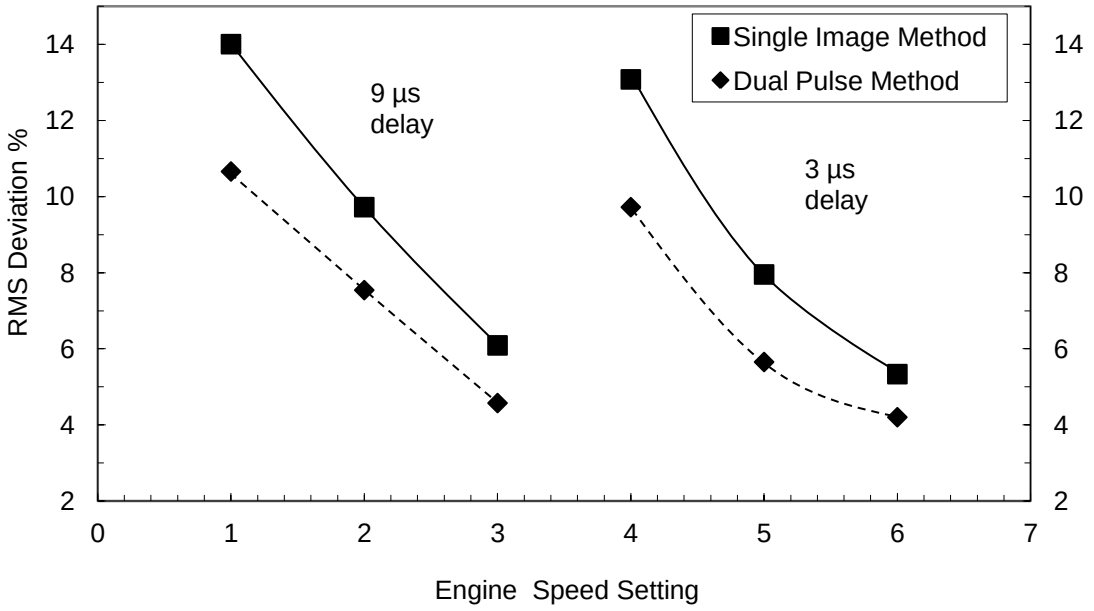

Figure 12. Comparison of dual-pulse and single-image method velocity deviation from the mean for J-85 jet engine.

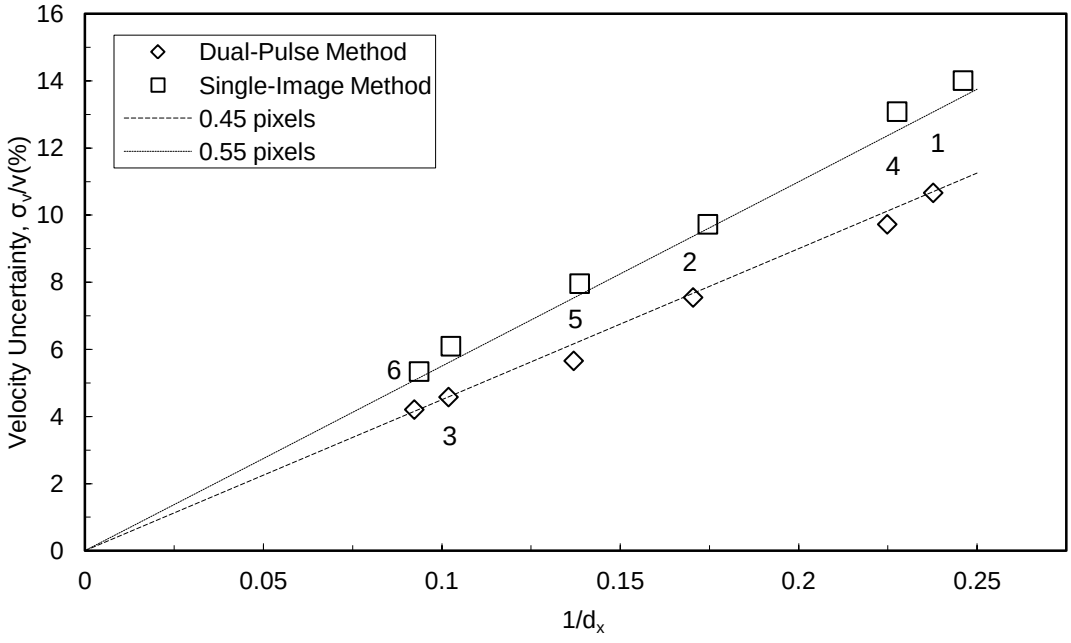

Figure 13. Velocity uncertainty from the mean derived from HTV data, where d_x is the average centerline displacement from Table 1.

2.6 Conclusion

The HTV method has been improved using a dual-pulse method that reduces the deleterious effects of vibration on the HTV measurement accuracy. The dual-pulse method is applied to a J85 jet engine exhaust to measure centerline velocities from 76 m/s at the lowest speed setting ramping up to 580 m/s at the highest speed setting. Using spatial correlation software, the velocities are measured from HTV images in spite of the low quality of the images. By using the dual-pulse feature of the intensified CCD camera, the measurement uncertainty was lowered about 20% (e.g. rms velocity deviation at full throttle decreased from 5% to 4%) when the vibration effect on displacement error was eliminated. The measured rms velocity deviations ranged from 4% to 14% and most of the rms velocity deviation is attributed to the measurement error in determining the displacement of the low signal images. Shorter grid displacements led to lower accuracy. Computer software developed by Gendrich and Koochesfahani (1999) determined the displacement in the images to about ±0.5 pixels. By analyzing the images with a single-image method and dual-pulse method, the rms value of the displacement was found to decrease from 0.55 to 0.45 pixels; this leads to an estimate of 0.3 pixels (~50 μm) rms deviation due to vibration when using the single-image method. Engine vibration also caused out of plane movement of the OH read sheet that led to displaced grid images that was not usable. With the 11x11 grid, multiple velocity vectors were obtained from a single image. By using the dual-pulse method in conjunction with the processing program, future studies can be done to efficiently determine velocities of other flows and devices.

CHAPTER III

Investigation of a Bow Shock Using HTV

3.1 Introduction

Molecular tagging velocimetry (MTV) is commonly used to characterize fluid flows (Wehrmeyer 1999; Pitz 2000; Lahr 2010; Barker 1998). MTV has been employed by several researchers to determine temperature and velocity in flows to characterize shock waves. Many of these methods include the use of Planar Laser-Induced Fluorescence (PLIF) to investigate oblique and bow shocks formed in cavities and around blunt and sharp-edged objects to simulate hypersonic flow for aerospace applications (Jeong 2008; Houwing 2001; Smith 1994; Ruyten 1998; Danehy 2001, 2003; Davidson 1991).

Previously, Smith et al. (1994) applied PLIF of NO to a shock tube flow with M_s of 2.0 and 2.5 for two conical test articles, one with a sharp tip and one blunt-nosed. The PLIF measurements were conducted as a preliminary means for demonstration, validation, and calibration of facility diagnostic systems such as planar temperature measurement. The experiment produced temperatures between 1000 and 1500 K. To further explore the shock tube flow, the present study employs HTV to determine the velocity downstream of the initial shock wave. The shock tube features pressure transducers which are used to determine shock speed. The HTV images are analyzed using a new template matching correlation technique (Ramsey 2011) to determine displacements of the grid intersections and thereby the two-dimensional velocity distribution downstream of the initial shock wave.

3.2 Experimental System

The HTV measurements were performed in a shock tube located at the Arnold Engineering Development Center, Arnold AFB, TN. The shock tube (Figure 14) has a 2.4-m driver section and a 4.5-m driven section with a 5.4-cm inner diameter. The shock tube was operated with a driver gas of helium for pressures between 2070 and 4820 kPa and a driven gas of moist air. The driven section is filled with moist air to improve signal quality. An aluminum diaphragm is located between the driver and driven section with a thickness of 1.575 mm. The shock tube features several pressure transducers. Pressure transducers K4 and K5 are used to determine the shock speed as well as trigger the

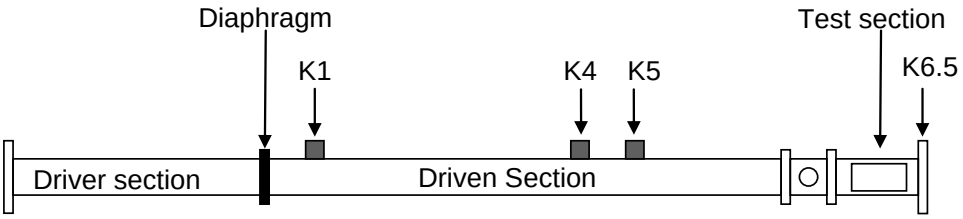

Figure 14. Side-view of shock tube. Pressure transducers K4 and K5 are used to determine shock speed. Laser beams are directed through the side of the test section window (100 mm x 20 mm).

system, while pressure transducer K1 is used only for triggering. The test section is located at the end of the driven section and contains four fused silica windows for interrogation. The laser sheet and grid were directed through a side window (100 x 20 mm). The test articles shown in Figure 15 include a cone model 10 mm in length with a 30-deg half-angle and a 17.8-mm long blunt nose model with a 10-deg half-angle. The test articles are fixed to the end of the shock tube via a 110-mm sting, and the flow is viewed from above through a 50 x 35 mm window on the top of the tunnel.

Figure 15. Test articles for experiment. Cone model (top) and blunt nose model (bottom). Each test article is attached to a 110 mm sting.

To interrogate the flow, a tunable 193-nm ArF excimer laser (Lambda Physik COMPex 150-T, 193-194 nm) with output energy of 150 mJ per pulse, 0.2 mrad divergence, and a pulse duration of 20 ns was used to photodissociate the water vapor to produce OH radicals. The ArF laser was operated in broadband mode at 193.4 nm (0.5 nm bandwidth). The ArF beam, 20 mm high by 10 mm wide, was split via a beam splitter. The split beam was sent into grid forming optics. The grid forming optics consist of two sets of optics closely spaced: a 300-mm focal length cylindrical lens (25 x 40 mm) and a stack of 11 cylindrical lenses (20 mm long x 2 mm wide). Each set of grid optics forms 11 parallel beams with exit energy of ~14mJ (~1.0 mJ/beam). The two sets of 11 beams are crossed at a 34 deg angle. The OH radicals were excited via an Nd:YAG (Continuum Lasers Powerlite 9010) pumped tunable dye laser with an ultraviolet wavelength extender. The doubled output of the dye laser is tuned to excite the strong $Q_1(1)$ line in the $A^2\Sigma^+(v'=1)\leftarrow X^2\Pi_i(v''=0)$ OH band at a wavelength of 281.997 nm (35461.330 cm^{-1}). The dye laser wavelength and the $Q_1(1)$ line position were determined by fluorescence excitation spectra taken in room air, as done previously (Blandford 2008; Alexander 2008). The ~282-nm beam (~8 mJ/pulse) was expanded by a negative

cylindrical lens (focal length ≅ -125 mm) and focused into a sheet 27 mm wide by 0.3 mm thick with a 500-mm focal length spherical lens.

The images were recorded using an intensified interline CCD camera (Princeton Instruments PI-MAX II 1024x1024 pixels). The fluorescence light was collected by a 105-mm focal length f/4.5 UV Nikon camera lens positioned 244 mm above the test section. To capture the OH fluorescence near ~305-325 nm and block interfering background light from the lasers (193-nm, 282-nm), a Schott UG-ll (1 nm thick) filter and a WG305 (3 mm thick) filter were used in front of the camera lens to create a bandpass filter from 305 to 375 nm. Figure 16 shows the laser pulse and camera gate timing from a typical shock tube run. The ArF laser pulse and Nd:YAG pulse are separated by a time of Δt=1 μs that sets the time of flight. The camera gate captures the delayed image after the shock has travelled past the test article but before the reflected shock travels back past the test article. The average undelayed image was generated by recording 100 grid images in room air before testing began at atmospheric pressure and averaging them. The camera image was calibrated by placing a ruler in the focal plane giving a factor of 34.71±0.25 pix/mm that is used to determine velocities. Thus, the laser line is about 11 pixels in diameter. The 1024 x 1024 pixel images correspond to a 29.5 x 29.5 mm area in the shock tube.

The synchronization of the laser and camera were controlled via a programmable experiment controller (LabSmith LC880) with ~17 ns jitter. Before the firing of the tunnel, the Nd:YAG laser is run at 10 Hz to ensure that it is at proper "warming conditions." Once the shock tube gasses are filled, a valve is opened and the shock begins its path. Once the shock passes pressure transducer K1 (Figure 14), the Nd:YAG

10-Hz pulse is inhibited and waits for the next triggering event created from pressure transducers K4 and K5. Pressure transducers K4 and K5 are used to create a dynamic delay; the LC880 uses the time for each and calculates a delay based upon this information to trigger the laser and camera system. The transducer signals, K4 and K5, are also recorded on an oscilloscope to be used to determine the shock speed. Figure 17 depicts the pressure transducer scope trace for a typical shot. The gradual increase in the signal is unexplained and should remain constant until the reflected shock is detected, but this increase may be due to drift caused by low insulation resistance, a characteristic of the piezoelectric pressure transducers. From this scope trace (Figure 17b) a time delay between transducers is extracted. With the known distance between the two transducers, the shock speed is determined for each shock tube run.

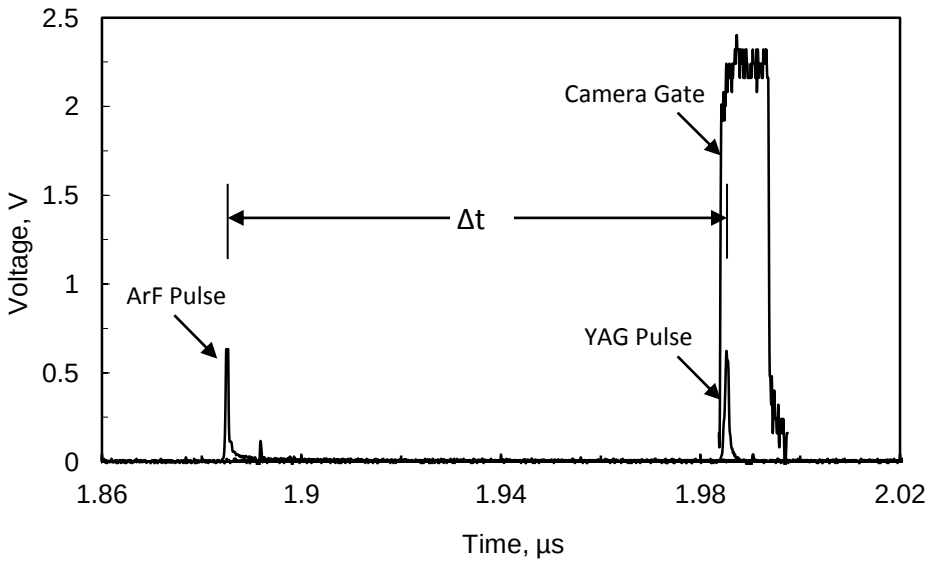

Figure 16. Laser pulse and camera gate timing from typical shock tube shot

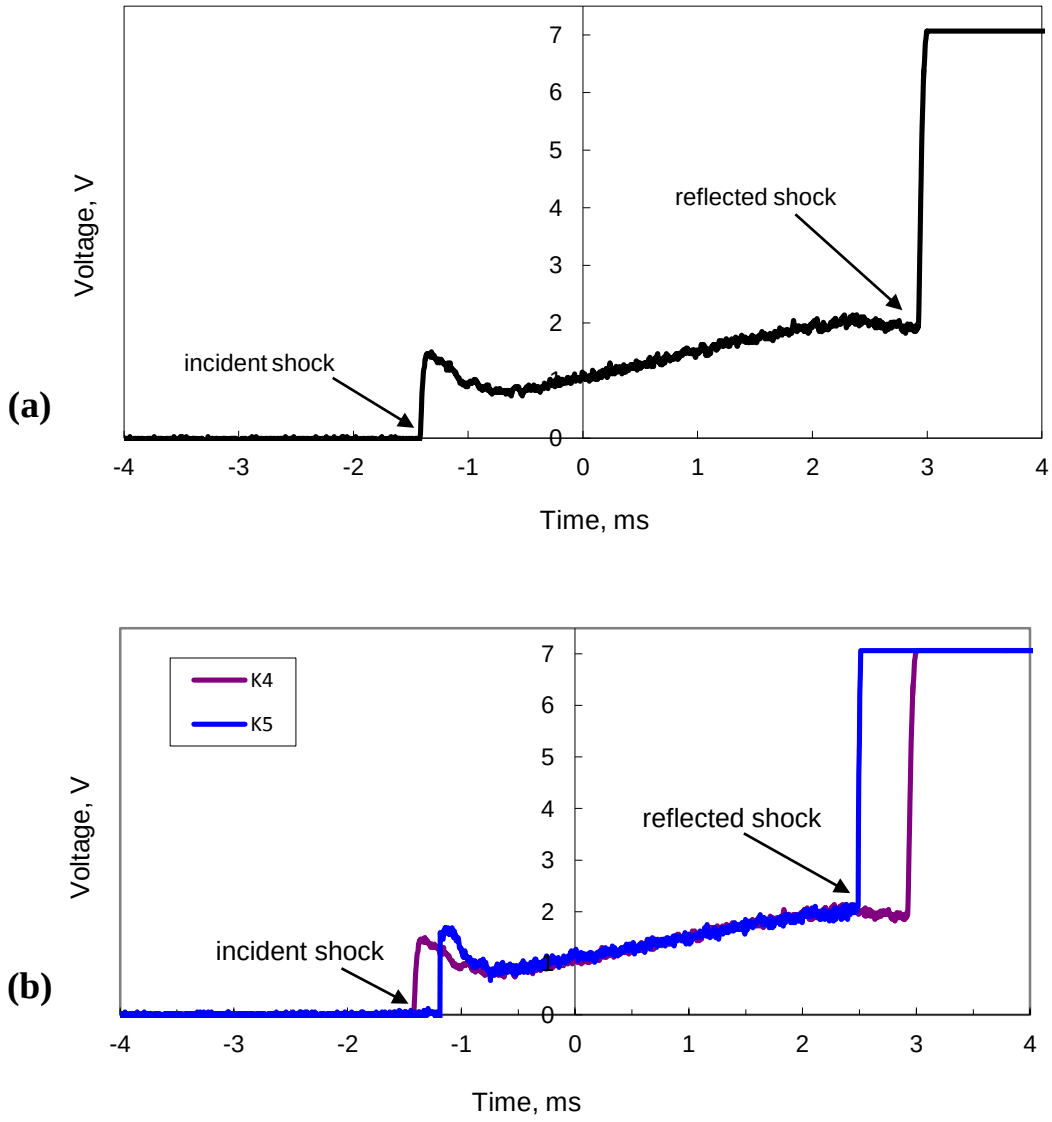

Figure 17. Pressure transducer scope traces (a) K4 scope trace to indicate incident and reflected shock location (b) K4 and K5 scope trace. K4 and K5 are used to determine incident shock speed.

To demonstrate the repeatability of the shock tube, the measured and calculated shock speeds are determined for comparison (Figure 18). The measured shock speed is determined from the aforementioned measurement via K4 and K5, while the calculated shock speed is determined from shock theory equation,

$$W_s = a_1\sqrt{\frac{\gamma_1+1}{2\gamma_1}\left(\frac{P_2}{P_1}-1\right)+1} \tag{4}$$

where the properties of air are assumed and the pressure ratio P_2/P_1 is determined from the initial driven and driver pressures, given by:

$$\frac{P_4}{P_1} = \frac{P_2}{P_1}\left\{1-\frac{(\gamma_4-1)(a_1/a_4)(P_2/P_1-1)}{\sqrt{2\gamma_1[2\gamma_1+(\gamma_1+1)(P_2/P_1-1)]}}\right\}^{-2\gamma_4/(\gamma_4-1)} \tag{5}$$

The pressure transducers do a relatively good job of determining shock speed. The outliers in Figure 18 are unexplained and may be due to non-ideal shock tube performance from a diaphragm that did not completely open.

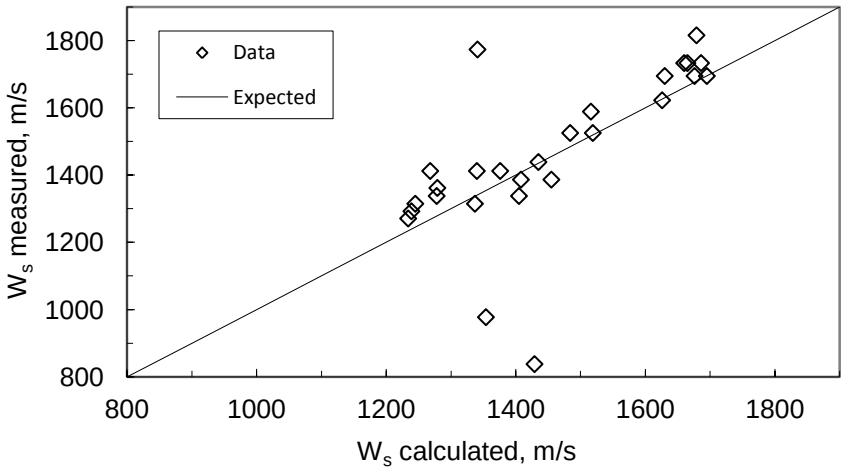

Figure 18. Measured and calculated shock speed comparison

3.3 Experimental Results

The experiment was conducted for three test conditions for each test article. Table 3 gives the measured time between pressure transducers K4 and K5, the measured and calculated shock speeds, and the pressure ratio derived from the measured shock speed. The calculated shock speed was derived from shock theory using the known driven and driver pressures. The pressure ratio was determined from the following 1D shock equation,

$$\frac{P_2}{P_1} = \frac{2\gamma_1}{\gamma_1 + 1}\left[\left(\frac{W_s}{a_1}\right)^2 - 1\right] + 1 \qquad (6)$$

assuming the properties of air. From this it can be inferred that pressure transducers K4 and K5 can measure the shock speed within 10% of what theory predicts if the extreme outliers in Figure 18 are ignored.

Table 3. Measured and calculated shock speed. The calculated shock speed is determined from P_4/P_1 using Equation 4 and 5. The pressure ratio P_2/P_1 is calculated from the measured shock speed using Equation 6. * Pressure, P_4 ,for test condition 6 could not be accurately determined.

	Measured $\Delta t_{K4\text{-}K5}$, μs	Measured W_s, m/s	P_2/P_1	P_4/P_1	Calculated W_s, m/s
Blunt Nose Model					
1	228	1340	17.4	113	1280
2	200	1530	22.7	243	1480
3	188	1620	25.7	425	1630
Cone Model					
4	216	1410	19.5	108	1270
5	208	1470	21.0	204	1440
6	214	1660	26.9	*	*

The HTV images were analyzed using a template matching method developed by Ramsey and Pitz (2011) to determine the displacements of the grid intersections. This automated code locates the grid intersections in each image by optimizing the correlation with a simulated surface (or template) defined by the sum of two Gaussian prisms corresponding to the two laser lines. The simulated surface has six degrees of freedom which are optimized for each intersection, including two location coordinates, the angle of each line, the Gaussian width of the two lines (assumed equal), and the relative intensity of the two lines. After all intersections are fit, corresponding intersection parameters in each undisplaced/displaced image pair are compared, and both linear and angular displacements can be determined. Dividing these by the known delay time Δt yields 2D velocity and two of its directional derivatives, along with information on signal and noise levels. In the current study, the angular degrees of freedom were not utilized since there is very little angular movement in the grid. When compared to the direct spatial correlation method employed by Gendrich and Koochesfahani (1999), the template method has improved results for the low resolution images typically used in HTV (Ramsey 2011).

The recorded HTV images are used to determine the gas velocity downstream of the shock wave, u_p. This experimental value is compared to theoretical value of u_p calculated from the pressure ratio determined from the measured shock speed according to the 1D shock relation:

$$u_p = \frac{a_1}{\gamma_1}\left(\frac{P_2}{P_1} - 1\right)\left(\frac{\frac{2\gamma_1}{\gamma_1 + 1}}{\frac{P_2}{P_1} + \frac{\gamma_1 - 1}{\gamma_1 + 1}}\right) \tag{7}$$

3.3.1 Blunt Nose Model

Figure 19 shows the undisplaced image and displaced image for shot 3 for the blunt nose model. The grid is positioned such that both the velocity in front and behind the shock can be visualized. The undisplaced image (Figure 19a) is imaged in room air at standard temperature and pressure before the experiment is begun; this method is used since vibration is not of major concern. The bright dots are where the laser beams hit the model surface. The displaced image (Figure 19b) shows the defined shock front as the shock passes the test article as the HTV grid is much brighter in the region behind the shock. By using the time delay of 1±0.05 μs between the firing of the lasers and the displacement between the undisplaced and displaced image, an average freestream velocity of u_p=1690 m/sec is determined. Also from this image one can infer in the postshock region that there is a temperature increase indicated by an increase in OH LIF signal behind the shock.

The velocity vectors that result from determining displacements in Figure 19 are shown in Figure 20 along with the shock front. The vectors indicate that the velocity is largest ahead of the shock front and then slows behind the shock. This result is also shown in Figure 21, with a minimum average value of 1250 m/sec behind the shock.

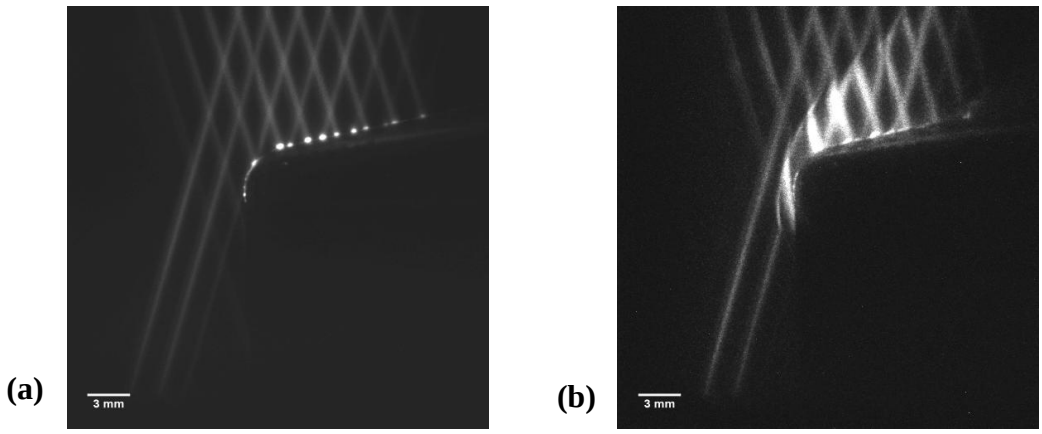

Figure 19. Undisplaced (a) and displaced image (b) pair for shot 3 for the blunt nose model with a measured free stream velocity of 1690 m/s. Image area: 29.5 mm x 29.5 mm.

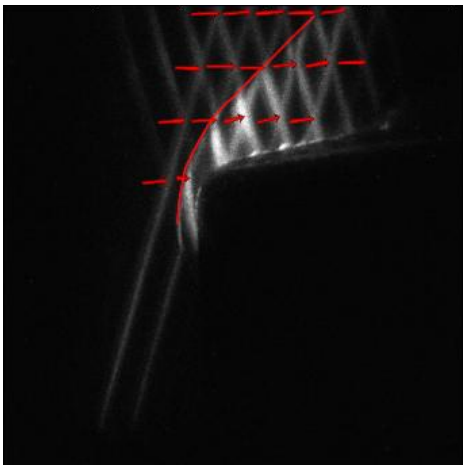

Figure 20. Velocity vectors for blunt nose model shot 3 superimposed on the displaced image. Image area: 29.5 mm x 29.5 mm.

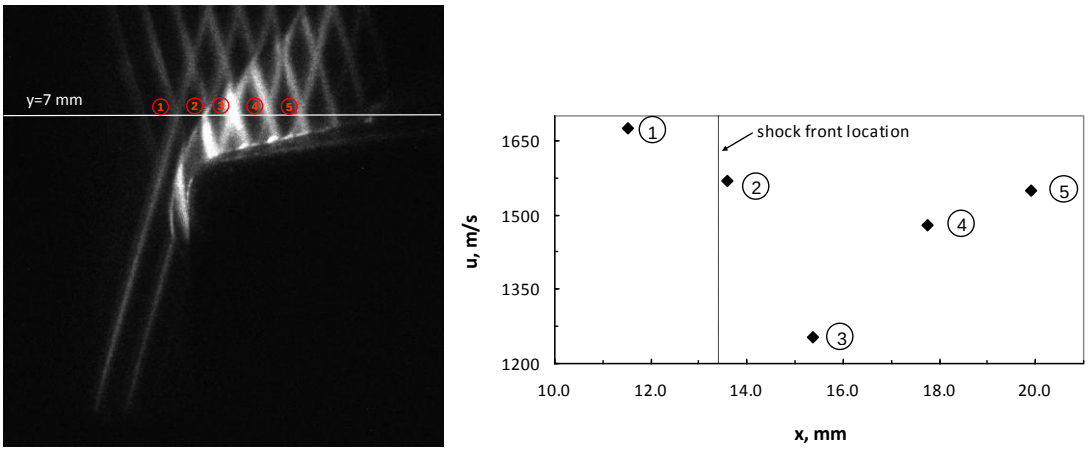

Figure 21. Velocity line out of blunt nose model image for shot 3 at y=7 mm. The circled numbers indicate the crossing location for each measurement. Image area: 29.5 mm x 29.5 mm.

The average freestream velocity of 1690 m/s measured from Figure 20 is not in good agreement with the predicted freestream velocity, u_p, as shown in Figure 22. In this figure, a comparison between the measured (1690 m/s) and calculated (1290 m/s) velocity downstream of the shock is given. The data shows as much as a 27% difference between the calculated and measured velocities. This difference may be due to 3D shock wave and boundary layer effects in the small diameter shock tube (5.4 cm). Because of wall viscous effects, a boundary layer forms behind the incident shock wave; this boundary layer increases shock attenuation and related nonuniformities (Peterson 2003; Mirels 1966). In this small (5.4 cm) diameter shock tube over the distance of the model, the limiting separation distance described by Mirels (1966) has not been obtained. Prior to the establishment of this condition, the shock has decelerated from some peak value. This deceleration results in an entropy variation which tends to create an increase in flow properties (Mirels 1966).

To complete the analysis of the blunt nose model, the stand-off distance Δd at the stagnation point of the blunt nose model for the three shock tube shots is displayed (Figure 23). From this plot it is confirmed that as the Mach number is decreased, the stand-off distance is increased, indicating a shock that is becoming increasingly detached as shown by Satheesh et al. (2007).

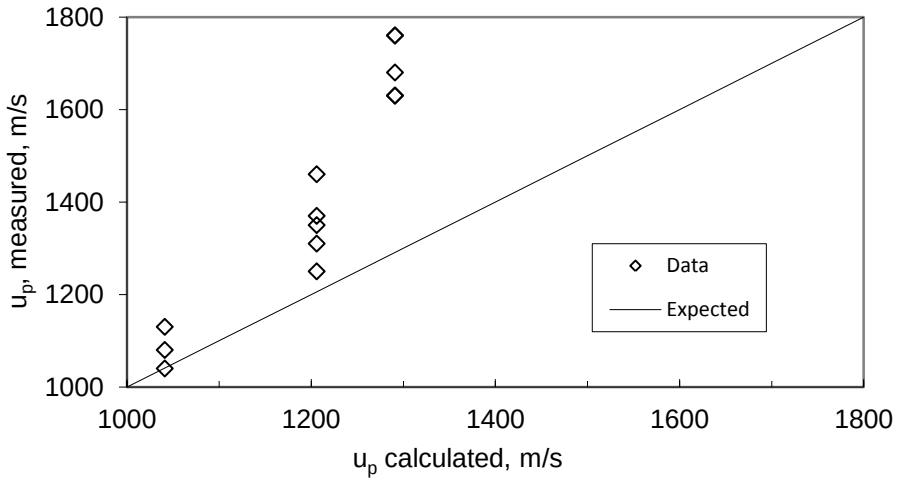

Figure 22. Measured and calculated velocity downstream of shock for blunt nose model.

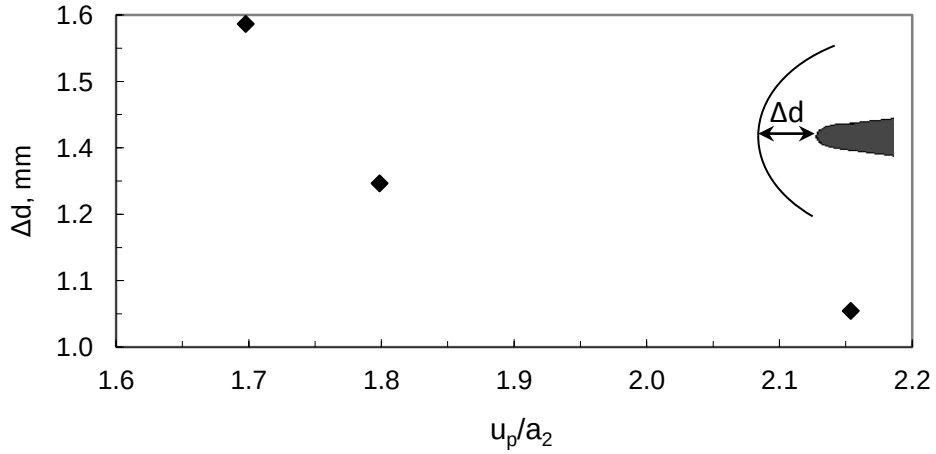

Figure 23. Standoff distance, Δd, from the stagnation point of the blunt nose model for the three shock tube shots.

3.3.2 Cone Model

The experiment was also conducted on a 30 degree half-angle cone model (Figure 15). The cone model's undisplaced and displaced images are displayed in Figure 24. Again, the average undisplaced image is obtained before the experiment is begun and is used to determine displacement. With the given time delay and displacement, an average freestream velocity of 1610 m/sec is calculated which compares to 1320 m/s from Equation 7. The resulting velocity vectors are displayed in Figure 25 along with the shock front. The velocity ahead of the shock has the highest speed and slows past the shock. The velocity behind the shock not only slows, but also contours away from the cone model. As with the blunt nose model, the measured and calculated freestream velocities produced by the incident shock wave do not closely lie with theory. However, for the cone model data set, HTV measurements of freestream velocity are closer to those predicted by Equation 7 as seen in Figure 26. Since this model has a sharp edge, versus the blunt edge of the previous model, the shock is attached and a shock angle can be determined. In Figure 27 the wave angle is plotted versus the measured shock speed, where the calculated wave angle is determined using the shock speed and shock properties curve, Chart 5, from NACA Report 1135 (1953). According to the theoretical calculations and as indicated by the calculated data set, the wave angle should decrease with increasing shock speed. As shown, there is a 14% difference between the measured and calculated values of the wave angle, except in the first data point. This difference is consistent with a higher freestream velocities found in the measurement. This data point may be attributed to random disturbances caused by the shock tube firing

that may have displaced the model away from the shocktube centerline to result in an incorrect angle measurement.

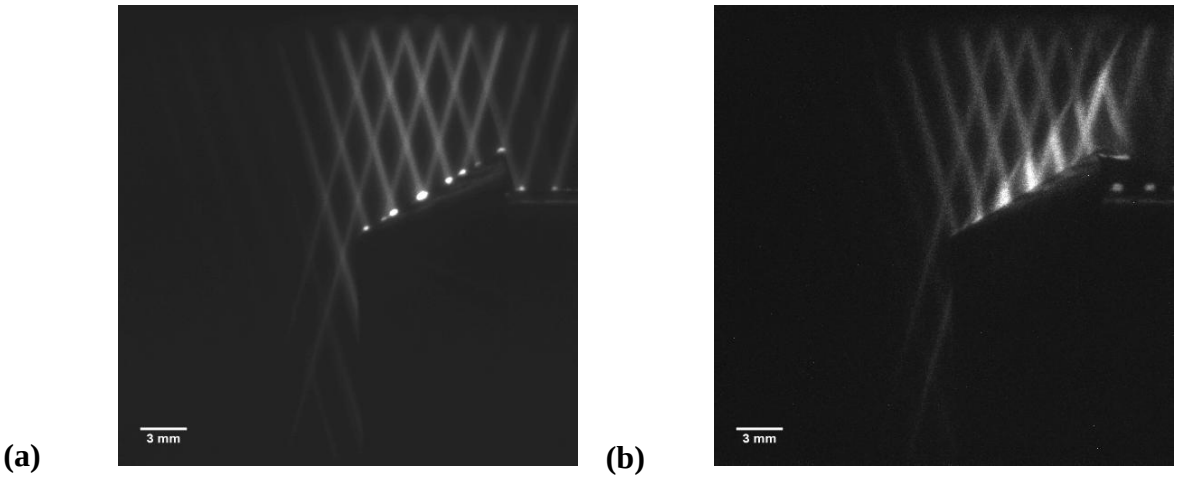

Figure 24. Undisplaced and displaced image pair for shot 6 for the cone model with a measured shock speed of 1660 m/s. Image area: 29.5 mm x 29.5 mm.

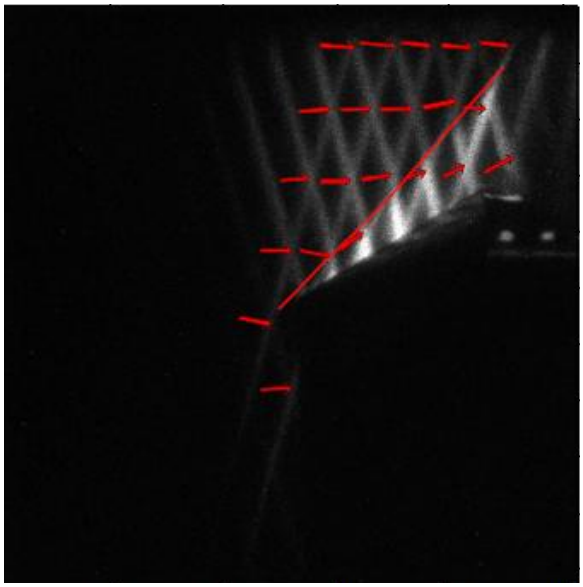

Figure 25. Velocity vectors for cone model shot 6 superimposed on the displaced image. Image area: 29.5 mm x 29.5 mm.

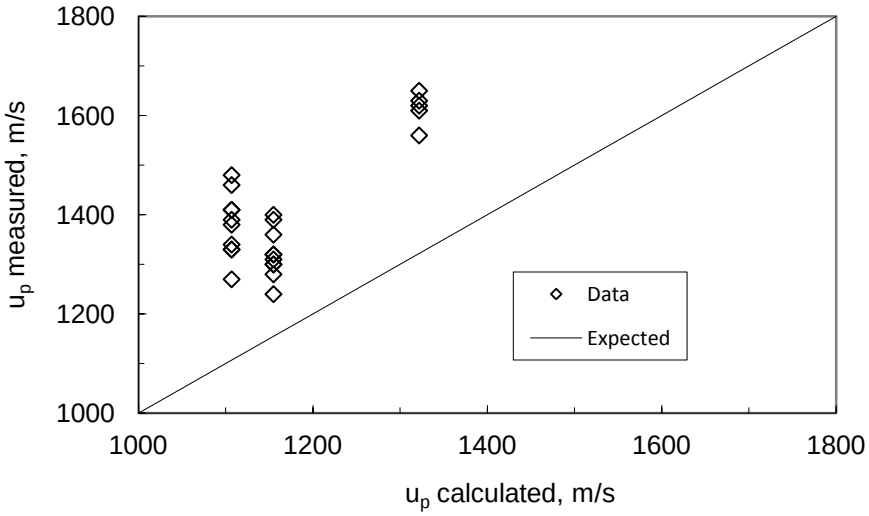

Figure 26. Measured and calculated velocity downstream of shock for the cone model

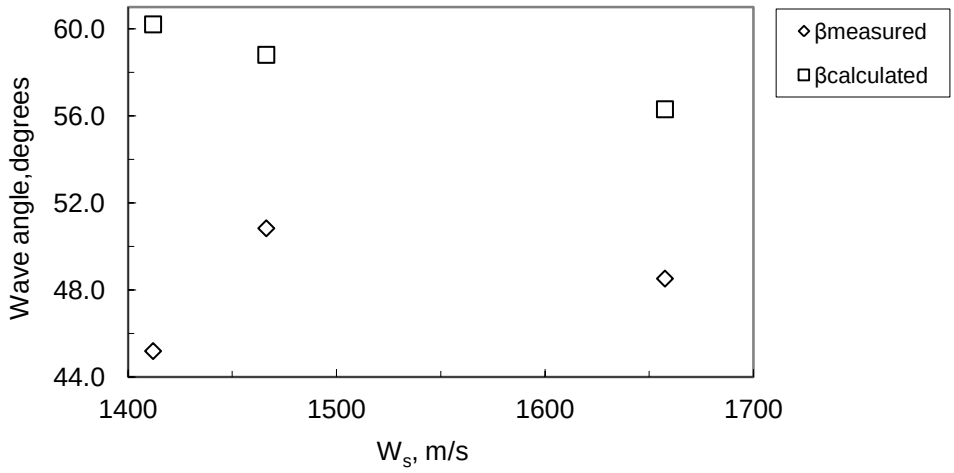

Figure 27. Measured and calculated wave angle for the cone model

3.4 Conclusion

HTV has been demonstrated in a high-speed flow using a grid that provides 2D velocity data. The use of the 11 x 11 grid allows for multiple velocity vectors to be obtained from a single image. The method was applied to two test articles, a blunt nose model and a cone model, to determine the velocity of the gas downstream of the shock wave. Measurements of the induced velocity, u_p, of the gas downstream of the incident shock are as high as 1690 m/sec but vary from the theoretical values by as much as 27%. By utilizing the installed pressure transducers along the shock tube, the shock speed can be determined within 10% of theoretical values, validating their use to derive the pressure ratio and other calculated quantities. Although the measured shock speeds reliably align with the theory, the induced velocity downstream of the shock does not. This can be attributed to the 1D shock theory used not taking into account 3D effects or boundary-layer growth in the small diameter shock tube (5.4 cm). By implementing more complex theoretical analysis, accounting for the 3D body, the aforementioned measurements can provide a means for validating theoretical codes and CFD.

REFERENCES

Alexander, A., J. Wehrmeyer, W. Runge, B. Blandford, A.V. Anilkumar and R. Pitz (2008). "Nonintrusive measurement of gas turbine exhaust velocity using hydroxyl tagging velocimetry," 26th AIAA Aerodynamic Measurement Technology and Ground Testing Conf., Paper No. AIAA-2008-3209, Seattle, WA.

Barker, P.F., A.M. Thomas, T.J. McIntyre and H. Rubinsztein-Dunloop (1998). "Velocimetry and thermometry of supersonic flow around a cylindrical body," AIAA Journal 36: 1055-1060.

Blandford, B.T., W.O. Runge, S. Hu, A.V. Anilkumar, R.W. Pitz and J. A. Wehrmeyer (2008). "Application of hydroxyl tagging velocimetry (HTV) to measure centerline velocities in the near field exhaust of a gas turbine engine," 46th AIAA Aerospace Sciences Meeting, Reno, Paper No. AIAA-2008-0235, Reno, NV.

Danehy, P.M., P. Mere, M.J. Gaston, S. O'Byrne, P.C. Palma and A.F.P. Houwing (2001). "Fluorescence velocimetry of the hypersonic, separated flow over a cone," AIAA Journal 39: 1320-1328.

Danehy, P.M., S. O'Byrne, A.F.P. Houwing, J.S. Fox and D.R. Smith (2003). "Flow-tagging velocimetry for hypersonic flows using fluorescence of nitric oxide," AIAA Journal 41: 263-271.

Davidson, D.F., A.Y. Chang, M.D. DiRosa and R.K. Hanson (1991). "Continuous wave laser absorption techniques for gas dynamic measurements in supersonic flows," Applied Optics 30: 2598-2608.

Fajardo, C. and V. Sick (2009). "Development of high-speed UV particle image velocimetry technique and application for measurements in internal combustion engines," Experiments in Fluids 46: 43-53.

Gendrich, C.P. and M.M. Koochesfahani (1999). "A spatial correlation technique for estimating velocity fields using molecular tagging velocimetry (MTV)," Experiments in Fluids 22: 67-77.

Gere, J.M. and S.P. Timoshenko (1997). "Mechanics of Materials," 4th Edition, Boston: PWS Publishing Company.

Houwing, A.F.P., D.R. Smith, J.S. Fox, P.M. Danehy and N.R. Mudford (2001). "Laminar boundary layer separation at a fin-body junction in a hypersonic flow," Shock Waves 11: 31-42.

Hsu, A.G., R. Srinivasan, R.D.W. Bowersox, S.W. North (2009). "Molecular tagging using vibrationally excited nitric oxide in an underexpanded jet flowfield," AIAA Journal 47: 2597-2604.

Ismailov, M.M, H.J. Schock and A.M. Fedewa (2006). "Gaseous flow measurements in an internal combustion engine assembly using molecular tagging velocimetry," Experiments in Fluids 41: 57-65.

Jeong, E., S. O'Byrne, I.S. Jeung and A.F.P. Houwing (2008). "Investigation of supersonic combustion with angled injection in a cavity-based combustor," Journal of Propulsion and Power 24: 1258-1268.

Lahr, M.D., R.W. Pitz, Z.W. Douglas and C.D. Carter (2010). Hydroxyl tagging velocimetry measurements of a supersonic flow over a cavity," Journal of Propulsion and Power 26: 790-797.

Lee, M.P. and R.K. Hanson (1986). "Calculations of O_2 absorption and fluorescence at elevated temperatures for a broadband argon-fluoride laser source at 193 nm," Journal of Quantitative Spectroscopy and Radiative Transfer 36: 425-440.

Miles, R.B., J. Grinstead, R.H. Kohl and G. Diskin (2000). "The RELIEF flow tagging technique and its application in engine testing facilities and for helium-air mixing studies," Measurement Science and Technology 11: 1272-1281.

Mirels, H. (1966). "Flow nonuniformity in shock tubes operating maximum test times," The Physics of Fluids 9: 1907-1912.

Mittal, M., R. Sadr, H.J. Schock, A. Fedewa and A. Naqwi (2009). "In-cylinder engine flow measurement using stereoscopic molecular tagging velocimetry (SMTV)," Experiments in Fluids 46: 277-284.

NACA (1953). Report 1135 Equations, Tables, and Charts for Compressible Flow. Report 1135, Ames Aeronautical Laboratory, Moffett Field, CA.

Peterson, E.L. and R.K. Hanson (2003). "Improved turbulent boundary-layer model for shock tubes," AIAA Journal 41: 1314-1322.

Pitz, R.W., J.A. Wehrmeyer, L.A. Ribarov, D.A. Oguss, F. Batliwala, P.A. DeBarber, S. Deusch and P.E. Dimotakis (2000). "Unseeded molecular flow tagging in cold and hot flows using ozone and hydroxyl tagging velocimetry," Measurement Science and Technology 11: 1259-1271.

Pitz, R.W., M.D. Lahr, Z.W. Douglas, J.A. Wehrmeyer, S. Hu, C.D. Carter, K.Y. Hsu, C. Lum and M.M. Koochesfahani (2005). "Hydroxyl tagging velocimetry in a supersonic flow over a cavity," Applied Optics 44: 6692-6700.

Ramsey, M.C. and R.W. Pitz (2011). "Template matching for improved accuracy in molecular tagging velocimetry," Experiments in Fluids 51: 811-819.

Ribarov, L.A., J.A. Wehrmeyer, R.W. Pitz and R.A. Yetter (2002). "Hydroxyl tagging velocimetry (HTV) in experimental airflows," Applied Physics B 74: 175-183.

Ribarov, L.A., S. Hu, J.A. Wehrmeyer and R.W. Pitz (2005). "Hydroxyl tagging velocimetry method optimization: signal intensity and spectroscopy," Applied Optics 44: 6616-6626.

Ruyten, W.M., M.S. Smith, L.L. Price and W.D. Williams (1998). "Three-line fluorescence thermometry of optically thick shock-tunnel flow," Applied Optics 37: 2334-2339.

Satheesh, K., G. Jagadeesh and K.P.J. Reddy (2007). "High speed schlieren facility for visualization of flow fields in hypersonic shock tunnels," Current Science 92: 56-60.

Sijtsema, N.M., N.J. Dam, J.H. Klein-Douwel and J.J. ter Meulen (2002). "Air photolysis and recombination tracking: a new molecular tagging velocimetry scheme," AIAA Journal 40: 1061-1064.

Smith, M.S., W.D. Williams, L.L. Price and J.H. Jones (1994). "Shocktube planar laser induced fluorescence measurements in support of the AEDC impulse facility," 18th AIAA Aerospace Ground Testing Conference, Paper No. AIAA-94-2649, Colorado Springs, CO.

Stier, B. and M.M. Koochesfahani (1999). "Molecular tagging velocimetry (MTV) measurements in gas phase flows," Experiments in Fluids 26: 297-304.

Timmerman, B.H., A.J. Skeen, P.J. Bryanston-Cross and M.J. Graves (2009). "Large-scale time-resolved digital particle image velocimetry (TR-DPIV) for measurement of high subsonic hot coaxial jet exhaust of a gas turbine engine," Measurement Science and Technology 20: 074002 (15pp) DOI 10.108810957-0233/20171074002.

Wehrmeyer, J.A., L.A. Ribarov, D.A. Oguss and R.W. Pitz (1999). "Flame flow tagging velocimetry with 193-nm H_2O photodissociation," Applied Optics 38: 6912-6917.